Materials Horizons

ROYAL SOCIETY OF CHEMISTRY

COMMUNICATION

View Article Online
View Journal | View Issue

Check for updates

Cite this: *Mater. Horiz.*, 2025, **12**, 10124

Received 5th June 2025,
Accepted 18th August 2025

DOI: 10.1039/d5mh01064k

rsc.li/materials-horizons

Breaking scaling relations in AgAuCuPdPt high-entropy alloy nanoparticles for CO_2 electroreduction *via* machine learning

Juan Manuel Arce-Ramos,[a] Quang Thang Trinh,[b] Zicong Marvin Wong,[a] Ben Wang,[c] Benjamin W. J. Chen,[a] Jia Zhang *[a] and Teck Leong Tan *[a]

CO_2 electroreduction is limited by linear scaling relationships that couple the stabilities of key intermediates (*COOH, *CHO) to CO adsorption, placing pure Cu catalysts at a volcano-plot ceiling of activity and selectivity. Here, we harness the compositional variety of nanosized AgAuCuPdPt high-entropy-alloy (HEA) particles to break these constraints. We trained an ultralight linear-regression surrogate (MAE ≈ 0.10 eV) based on density functional theory (DFT) calculations on CO adsorption configurations to screen millions of Monte-Carlo-generated local environments of a variety of HEA formulations in seconds. Sites with predicted CO adsorption energy in the optimal −0.6 to −0.4 eV window were probed explicitly for *COOH and *CHO adsorption. From this screening, we discovered a family of "special" sites—Au centers with coordination number 8 (CN = 8) neighbored by corner Cu atoms of CN = 6—that stabilize bidentate binding of *COOH and *CHO. This lowers the potential-limiting *CO → *CHO step to ∼0 eV, and decisively breaks the scaling relations between CO* and CHO*. Our two-tier machine-learning + DFT workflow identifies active sites on HEAs that outperform the single-metal volcano limit and provides a transferable roadmap for the rational design of next-generation CO_2RR electrocatalysts *via* tuning of the active site composition.

New concepts

We present a two-tier framework that bridges rapid compositional screening to mechanistic insights for alloy electrocatalysts, using CO_2-to-CH_4 conversion as a case study. Tier 1 employs an ultralight machine-learning (ML) surrogate, trained on a few hundred DFT CO-adsorption data points, to predict CO adsorption energy for any local motif in nanoscale AgAuCuPdPt high-entropy alloys. Monte-Carlo sampling then scans millions of possible surface arrangements across hundreds of bulk compositions in minutes. Tier 2 augments these statistical insights with targeted DFT calculations on the key *COOH and *CHO intermediates. This combined analysis uncovers an unrecognized active motif: an Au surface atom (CN = 8) adjacent to a Cu corner atom (CN = 6). The bimetallic site breaks the conventional CO–CHO scaling relationship, drives the rate-limiting *CO → *CHO step to near thermoneutrality, and outperforms the single-metal volcano limit. Composition maps reveal that increasing Au and reducing Pd/Pt maximizes the density of such motifs. By integrating random-site statistics, descriptor-based ML, and mechanistic DFT calculations, our approach delivers actionable design rules (composition and local coordination, intrinsically linked to particle size) applicable to other complex alloy catalytic materials.

1. Introduction

Electrochemical CO_2 reduction reaction (CO_2RR) offers a promising route for mitigating greenhouse gas emissions while producing valuable fuels and chemicals. Pioneering work by Hori and co-workers demonstrated that copper (Cu) catalysts can convert CO_2 into CO and various hydrocarbons, including methane, C1 and C2 products.[1,2] Since then, copper-based systems have been among the most widely studied catalysts for CO_2RR. In fact, sixteen different products can form on a pure Cu surface.[3] Commercial deployment, however, remains at the pilot plant stage. Future electrolyzers will need to run at voltages lower than 3 V and current densities greater than 200 mA cm^{-2} to be economically viable.[4] Cu-based catalysts not only struggle to meet these voltage and current targets but also suffer from selectivity issues which severely hinder industrial viability. In practice, CO_2 feedstocks can come from concentrated point sources (*e.g.*, power plants or chemical facilities)[5] or from direct air capture; the latter is substantially more energy- and cost-intensive due to the dilute atmospheric concentration.[6]

A key limitation is that Cu already sits near the peak of the activity-volcano curve, a computational screening framework

[a] *Institute of High Performance Computing (IHPC), Agency for Science, Technology and Research (A*STAR), 1 Fusionopolis Way, #16-16 Connexis, Singapore 138632, Republic of Singapore. E-mail: tantl@ihpc.a-star.edu.sg, zhangj@ihpc.a-star.edu.sg*
[b] *Queensland Quantum and Advanced Technologies Research Institute, Griffith University, Nathan, Queensland 4111, Australia*
[c] *Department of Materials Science and Engineering, National University of Singapore, Singapore 117575, Singapore*

based on adsorbate binding energies popularized by Nørskov *et al.*[7] Cu binds CO just strongly enough to balance the adsorption and desorption of the key reaction intermediates. Notably, the binding energies of key intermediates (like *COOH or *CHO) correlate linearly with that of CO because they conserve the same metal–C bond but differ only by an attached or protonated oxygen-containing group.[8] Therefore, their adsorption energies change nearly proportional to E_{ads}(CO). These scaling relationships render further activity improvements beyond the volcano apex theoretically impossible and breaking them has become a central focus to surpass the fundamental limitations.[9,10]

High-entropy alloys (HEAs) have recently emerged as promising electrocatalysts because they provide a wide compositional design space for tuning their electronic structures that could potentially break away from the conventional linear scaling relationships[11–13] and, in some cases, deliver superior activity compared to single-metals or simpler binary alloys. For CO_2RR, an equiatomic AgAuCuPdPt HEA outperformed pure Cu catalysts.[14] Similar performance boosts have been reported for ammonia decomposition,[15] oxygen reduction reaction (ORR),[16] and hydrogen evolution reaction (HER),[17] where promising HEA compositions had been identified to outperform conventional metal ordinary alloy systems. Fig. 1 provides a schematic of the electrochemical cell, indicating HEA use at the cathode and summarizing the overall reactions mentioned (CO_2RR, ORR, OER). Nevertheless, the vast number of possible local configurations in a HEA obscures clear structure–activity relationships and complicates analysis. It remains uncertain whether their enhanced performance stems from breaking adsorption scaling relationships or a coincidental combination of conventional effects.

In addition to composition, particle size is another critical variable in electrocatalysis. As metallic particles shrink into the few-nanometer regime, activity often rises—not merely because of higher surface-to-volume ratios but also owing to a surge in low-coordination edge and corner atoms. These under-coordinated sites generally increase reactivity, accelerating turnover and redirecting reaction pathways. For instance, a systematic study on 2–15 nm Cu nanoparticles showed a dramatic activity increase as size decreased, but hydrocarbon selectivity (CH_4, C_2H_4) fell once the fraction of low coordination sites became dominant, favoring HER and CO formation instead of CO hydrogenation.[18] Similar size effects have been predicted for HEA nanoparticles in a combined density functional theory (DFT)-experiment work.[19] They reported that smaller HEA particles are more active for HER and ORR, and DFT indicates the same trend for the initial CO_2 → *COOH step—even though *CO → *CHO can become rate-limiting depending on the transition metal. Despite their potential, truly nanoscale HEA catalysts remain under-explored because their synthesis is more challenging than that of conventional monometallic or bimetallic nanoparticles.[20]

Here, we combine DFT with a lightweight machine-learning (ML) surrogate model to navigate the large design space of ~1 nm AgAuCuPdPt nanoparticles. We aim to harness both nanosize effects and multielement synergy to boost CO_2RR activity and selectivity. We first use a well-established descriptor, the adsorption energy of CO molecule (E_{ads}(CO)), which correlates with *COOH and *CHO stabilities on single-metal surfaces, to train a linear regression model on a curated DFT data set. We then applied this surrogate to screen millions of Monte-Carlo-generated local motifs across hundreds of AgAuCuPdPt compositions, reducing the screening task from months of DFT time to minutes. This screening showed that increasing the Au content most effectively raises the fraction of sites in the Sabatier "sweet-spot" window (−0.6 to −0.4 eV). Building upon these insights, we examined explicitly for *COOH and *CHO adsorption *via* higher fidelity DFT simulations. This two-tier strategy pinpoints a family of Au-centered active sites with coordination number (CN) of 8, flanked by Cu corner atoms with CN = 6. Detailed DFT calculations show that these Au(CN = 8)–Cu(CN = 6) pairs stabilize bidentate binding of *COOH and *CHO, break the conventional CO–CHO scaling line, and render the rate-limiting step thermoneutral or even exothermic. In contrast, Pd and Pt neighbors bind both CO and H too strongly, favoring the competing HER instead. By coupling rapid ML screening with targeted mechanistic analysis *via* DFT, we thus demonstrate how compositional complexity and tailored local coordination in HEAs can unlock catalytic sites that outperform the single-metal volcano limit—providing a clear recipe for the rational design of next-generation CO_2RR electrocatalysts. The emphasis throughout this work is on rapid, physics-based screening and atomic-level design rules. Investigation of long-term electrochemical durability and scale-up are beyond our present scope and are flagged for future explorations.

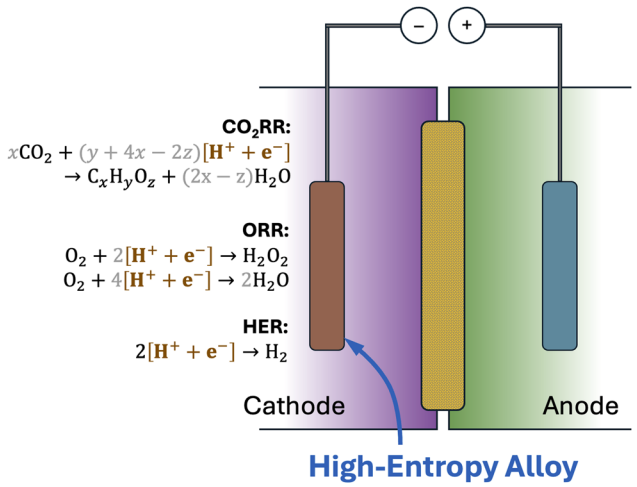

Fig. 1 Schematic electrochemical cell highlighting a high-entropy-alloy (HEA) cathode and the overall reactions for CO_2RR, ORR, and HER.

2. Methodology

2.1. DFT calculations

The structural optimization and stability energy of the nanoparticle models as well as adsorption configurations were carried out *via* DFT calculations using VASP with the projector

augmented-wave (PAW) method[21] and a plane-wave cutoff energy of 500 eV. We employed the generalized gradient approximation (GGA) with the revised Perdew–Burke–Ernzerhof (RPBE)[22] exchange–correlation functional. Cu and equimolar AgAuCuPdPt HEA Icosahedral nanoparticles (NP) with 55 atoms were used as catalyst model. A vacuum region of 10 Å in all directions was applied around each nanoparticle structure, creating a 20 Å × 20 Å × 20 Å unit cell. This vacuum spacing prevents spurious interactions between periodic images in simulations, thereby allowing accurate assessment of the isolated nanoparticle's structural and electronic properties. The Brillouin-zone was sampled with a single k-point. Partial occupancies were treated with the Methfessel–Paxton scheme at a width of 0.1 eV. The self-consistent loop used an energy change threshold of 10^{-6} eV, and geometry optimizations employed a force convergence criterion of 10^{-2} eV Å^{-1}. We found negligible differences between spin-polarized and non-spin-polarized calculations, therefore, non-spin-polarized method was adopted. Gibbs free energies were obtained by correcting the DFT electronic energies with zero-point, thermal, and entropic contributions derived from vibrational frequencies calculated *via* the finite-difference method as implemented in VASP.

CO adsorption energies, E_{ads}(CO), were calculated for each site of the selected nanoparticles by placing a CO molecule above the target metal atom with the C–O axis aligned towards the NP's center. After optimization, E_{ads}(CO) was computed as E(total) − E(NP) − E(CO), where E(total) is the energy of the adsorbed system, E(NP) the energy of the NP, and E(CO) is the energy of gas-phase CO.

The formation energy of the various intermediates was derived from the following stoichiometric equation:

$$CO_2(g) + n[e^- + H^+] \rightarrow {}^*CO_{2-x}H_{n-2x} + xH_2O(g) \quad (1)$$

where x accounts for water formation during CO_2RR, and the energies of CO_2(g), [e^- + H^+], and H_2O(g) are taken as references. Accordingly, the formation energy of any intermediate in the CO_2RR is computed as:

$$E(*CO_{2-x}H_{n-2x}) = E(*CO_{2-x}H_{n-2x}) + xE(H_2O) - E(CO_2) - \frac{n}{2}E(H_2) \quad (2)$$

with $E(H_2)$ corresponding to the energy of gas-phase H_2 in agreement with the computational hydrogen electrode approach.[23] Therefore, the three relevant reaction energies, up to the formation of *CHO, can be computed in the following way:

$$\Delta E1 = E(*COOH) \quad (3)$$

$$\Delta E2 = E(*CO) - E(*COOH) \quad (4)$$

$$\Delta E3 = E(*CHO) - E(*CO) \quad (5)$$

2.2. Building AgAuCuPdPt HEA nanoparticles

To accurately model the complex structures of HEA nanoparticles, we employed the thermodynamic tool-kit (TTK) code to generate representative structural models of AgAuCuPdPt HEA nanoparticles[24–26] based on the special quasi-random (SQS) method.[27] The code had been used to study the structures of other high-entropy systems as well[28,29] *via* the cluster expansion approach.[30] This approach allows for the creation of nanoparticles that closely mimic the structural complexity of disordered HEAs by optimizing cluster correlation functions.[31,32] Among the various HEA configurations generated, we selected the single arrangement closest to a perfectly disordered HEA nanoparticle consisting of 55 atoms, with 11 atoms of each species. An icosahedral symmetry was chosen for the nanoparticle structure as it represents one of the most stable configurations for nanoparticles due to its ability to minimize surface energy.[33,34] This symmetry not only enhances structural stability but also maximizes the proportion of surface atoms, which is critical for catalytic performance since surface atoms are directly involved in adsorption and reaction processes. In addition, to comprehensively explore the configuration space of the HEA nanoparticle and capture the effects of atomic arrangement on catalytic properties, we permuted the five elemental labels (Ag, Au, Cu, Pd, Pt) in the chosen arrangement. This resulted in 5! = 120 unique elemental permutations, which allows us to systematically investigate how the local atomic environment influences properties such as adsorption energy and electronic structure. The thermodynamic stability and structural integrity of these permuted configurations were confirmed through full structural relaxation and a subsequent analysis of their formation energies and bond length distributions, as detailed in the SI (Section S1 and Fig. S1).

2.3. Linear model for CO adsorption prediction

Model features generation. To address the large number of unique binding sites in the HEA, we developed a linear model that predicts E_{ads}(CO) from local atomic environments. The model uses 15 features grouped into three categories:

1. M_i: binary variables indicating the metal at the adsorption site (where i is either Ag, Au, Cu, Pd, or Pt), directly binding the CO molecule. A value of 1 denotes the presence of a specific metal at the adsorption site, and 0 denotes its absence.

2. S_i: counts of surface atoms of each metal type neighboring the adsorption site.

3. B_i: counts of subsurface (bulk) atoms of each metal type neighboring the adsorption site.

This way the linear model with regression coefficients x_k becomes:

$$E_{ads}(CO) = x_0 + x_1M_{Ag} + x_2M_{Au} + x_3M_{Cu} + x_4M_{Pd} + x_5M_{Pt} + x_6S_{Ag} + x_7S_{Au} + x_8S_{Cu} + x_9S_{Pd} + x_{10}S_{Pt} + x_{11}B_{Ag} + x_{12}B_{Au} + x_{13}B_{Cu} + x_{14}B_{Pd} + x_{15}B_{Pt} \quad (6)$$

Fig. S2 illustrates how the feature values are assigned to the two adsorption site types in icosahedral nanoparticles, *i.e.*, edge and corner sites.

3. Results

3.1. CO_2-to-CH_4 mechanisms on Cu nanoparticles

For reference, we first investigated the CO_2-to-CH_4 mechanism on a Cu_{55} icosahedral NP; Fig. 2 reports the Gibbs free energies of all intermediates. The first proton-coupled electron transfer (PCET) step, $*CO_2 + [e^- + H^+] \rightarrow *COOH$, requires overcoming a 0.68 eV thermodynamic barrier. After *CO formation, obtained by $*COOH + [e^- + H^+] \rightarrow *CO + H_2O$, an exothermic step (−0.56 eV), the reaction can proceed *via* CHO* or COH*. The formation of *CHO from *CO has a 0.90 eV barrier, which is 0.28 eV lower than that required for *COH formation. Thus, *CHO formation is dominant and rate-limiting on the Cu_{55} NP. Considering the full pathway, the first and third steps (formation of *COOH and *CHO) are the most energy-intensive, and we will assume these are potential-limiting in the HEA NPs.

3.2. Prediction of CO adsorption on HEA nanoparticles

CO_2 conversion to CH_4 proceeds through several PCET steps, with the formation of *COOH and *CHO as the potential-limiting steps. On single-metal surfaces, these steps adhere to linear scaling relationships linking the stabilities of *COOH and *CHO, effectively capping the activity, beyond which, it would be challenging to improve both steps simultaneously.[35] HEAs provide multielement and diverse local site compositions to break these conventional scaling constraints. However, enumerating every possible adsorption site in a HEA nanoparticle—especially for *COOH and *CHO binding—is computationally prohibitive if approached solely *via* DFT. To address this complexity, we use CO adsorption as a practical surrogate for initial screening. Leveraging the approximate E_{ads}(CO)–(*COOH,*CHO) scaling, we rapidly exclude sites with excessively strong or weak CO binding. Once we have identified promising sites, we can perform more detailed DFT calculations on *COOH and *CHO to verify if the multielement synergy truly disrupts linear scaling and enhances activity.

By applying this multi-level approach, we leverage the efficiency of a linear regression model for E_{ads}(CO) to explore the immense configurational space of HEAs, then refine our understanding of the most promising local sites through targeted DFT calculations of *COOH and *CHO. This strategy balances computational feasibility with the potential for breakthrough performance in CO_2RR.

3.2.1. DFT-calculated CO adsorption. We initially performed DFT calculations of E_{ads}(CO) on distinct HEA nanoparticles, examining on-top binding sites. Because CO is experimentally found to adsorb preferentially on on-top positions on Ag, Au, Cu and Pt surfaces,[36] we limited our survey to on-top configurations. With this choice, we aim to preserve chemical fidelity while keeping the DFT workload manageable for a five-element HEA. Eight HEA NPs were selected to cover a whole range of stabilities within the 120 possible NP configurations (Fig. 3), see Methods Section for more details. Notably, we included metals Pt, Pd, Cu, Au, and Ag in equal compositions. Each icosahedral NP has 55 atoms (with 42 atoms on the surface), which led us to 336 possible adsorption sites for CO.

The resulting E_{ads}(CO) distribution (Fig. 3c) depends strongly on which metal atom directly binds CO, following the approximate trend Pt > Pd > Cu > Au > Ag. Nevertheless, each individual metal distribution spans a broad range of adsorption energies. For instance, the E_{ads}(CO) over Pt sites vary between −2.43 eV and −1.40 eV, illustrating that the local environment (*e.g.*, neighboring metals, coordination number) also significantly affects E_{ads}(CO). For reference, we examined a pure Cu_{55} NP, obtaining $E_{ads}(CO) \approx -0.86$ eV to −0.89 eV at Cu sites with CN of 8 and 6. Overall, the site-specific E_{ads}(CO) values on the HEA nanoparticles roughly follows the trend as those we computed for the corresponding pure-metal (111) surfaces, although the pure metals are systematically shifted toward weaker binding (Fig. 3c).

Volcano-plot and Sabatier analyses on step surfaces of various metals place the optimum CO binding energy close to the CO*|CO(g) thermodynamic equilibrium line at a CO partial pressure of 1%, $E_{ads}(CO) \sim -0.5$ eV.[35,37] Here we relax this theoretical optimum by ±0.1 eV and adopt −0.6 eV to −0.4 eV as practical target window for optimal CO_2RR-to-CH_4 selectivity. This range is approximate and meant only as a practical guideline: CO must bind strongly enough to be further hydrogenated to methane but not so strongly as to hinder product desorption or favor undesired side reactions. Within our

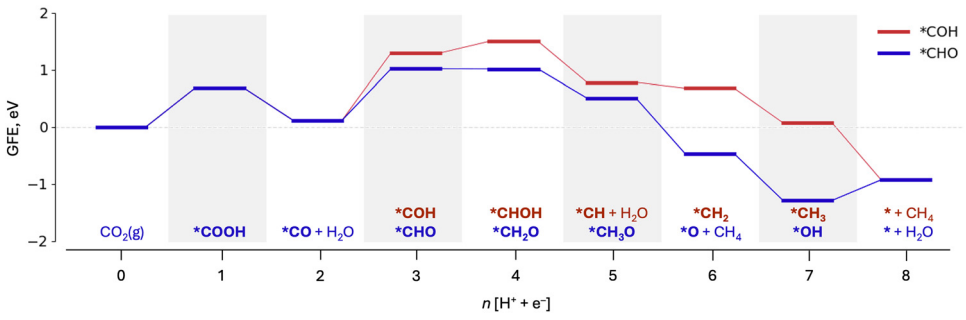

Fig. 2 Gibbs free energy diagram for the CO_2RR into methane through *CHO (blue) or *COH (red) intermediates on a Cu_{55} NP with reference to gas-phase CO_2 and H_2. The CO_2RR progresses through the reaction of the intermediates (as displayed with the blue or red labels) with the $H^+ + e^-$ pair. The total number of $H^+ + e^-$ pairs is displayed in the abscissa. The two reactions with the highest thermodynamic barriers are the PCET reactions $CO_2(g) + [e^- + H^+] \rightarrow *COOH$ and $*CO + [e^- + H^+] \rightarrow *CHO$.

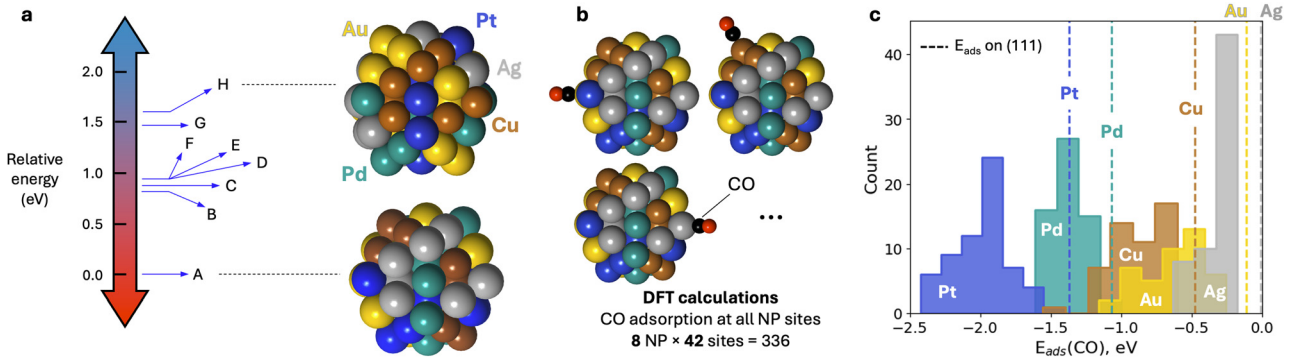

Fig. 3 (a) Eight AgAuCuPdPt HEA nanoparticle models (labels A–H) were considered spanning over a wide range of stabilities. (b) The adsorption of CO was considered only on on-top positions. (c) The DFT E_{ads}(CO) distribution of HEA NPs is shown where the nature of the adsorption metal strongly affects it. The dashed lines are our calculated E_{ads}(CO) on pure metal (111) surfaces.

dataset, Pt and Pd sites bind CO too strongly, whereas Ag, Au, and Cu can yield moderate binding energies, overlapping with the desired range.

3.2.2. Data filtering and feature definition. While the DFT calculations yielded 336 distinct CO adsorption configurations, a subset underwent large-scale structural rearrangements upon optimization. Among them, there were 23 configurations where CO moved to either a bridge or a 3-fold position during the structural relaxation. Because such configurations no longer reflect the initial on-top binding, they were filtered out (around 16% of the total) according to a restructuring criterion described in the SI. The final dataset contained 280 configurations.

We next built a linear regression model (eqn (6)) that uses local environment features to predict E_{ads}(CO). Each configuration is encoded by the identity of the binding metal and the elemental counts in its first coordination shell, explicitly separating surface and subsurface neighbors (Fig. 4a and Fig. S2). For more details, see the Methods section. This framework captures the identity and number of nearest neighbors around the binding site in a straightforward manner, providing local configurational/structural features for the regression.

After training on the 280 filtered configurations and their corresponding adsorption energies (E_{ads}(CO)), the model achieved a mean absolute error (MAE) of 0.100 eV (RMSE = 0.135 eV) and a coefficient of determination (R^2) of 0.9667 during cross-validation, Fig. 4b. The fitted coefficients are listed in Table S1. This high accuracy is especially noteworthy for a linear regression model, given that the state-of-the-art ML approaches have reported comparable errors. For example, Chen *et al.*[7] trained a neural network on DFT-derived data for predicting *CO adsorption energies, among other intermediates, obtaining MAE = 0.096 eV for CO adsorption.[11] In another study, Rittiruam *et al.*[33] evaluated multiple ML algorithms for CO adsorption and found that the Gaussian process regression yields RMSE = 0.06 eV.[38] The accuracy of our surrogate model indicates that these local environment descriptors effectively capture the key factors governing CO adsorption in the HEA. Moreover, the linear model's simplicity allows for rapid predictions of E_{ads}(CO) across an extensive range of potential sites—far beyond the reach of full DFT calculations.

We also tested a fast ML interatomic potential (uma-m-1p1 from the UMA's family of Meta FAIR)[39] for CO adsorption energy prediction. Against our DFT set (280 sites), UMA yielded

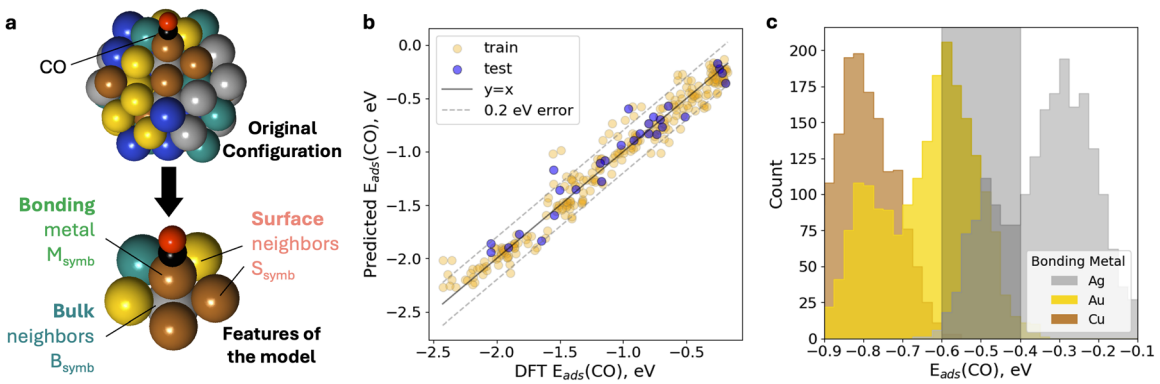

Fig. 4 (a) Adsorption site motif used to generate the features for the surrogate model (eqn (6)). (b) Parity plot comparing the predicted and DFT-calculated E_{ads}(CO). (c) Distribution of E_{ads}(CO) over all possible adsorption site ensembles formed on a AgAuCuPdPt HEA icosahedral 55-atom NP, enlarged at the region close to the ideal E_{ads}(CO) window between −0.60 eV and −0.4 eV.

MAE = 0.086 eV and RMSE = 0.165 eV with several clear outliers (Fig. S5). These models are promising screening accelerators, yet their accuracy still needs improvement and/or system-specific retraining before they can replace DFT. For large compositional scans, our linear surrogate remains orders-of-magnitude faster, evaluating millions of motifs in seconds.

3.2.3. Predicting CO adsorption in unseen configurations. To apply the surrogate model to realistic alloy formulations we generated, for each bulk composition, a representative surface population of on-top motifs by Monte-Carlo sampling (full protocol in Section S2 of the SI). Briefly, the surface atoms are partitioned into 30 edge positions (CN = 8) and 12 corner positions (CN = 6) of the 55-atom icosahedron (Fig. 4a) and were populated with Ag, Au, Cu, Pd, Pt in proportion to the prescribed bulk mole fractions. We explored two bulk-composition grids. In the first, Ag, Au, and Cu contents varied from 0 to 60 at% in steps of 5 at%, with Pd = Pt = 20 at% for a total of 91 formulations. In the second, Ag, Au, and Cu ranged from 0 to 90 at% in steps of 5 at%, with Pd = Pt = 5 at% for a total of 190 formulations. For every HEA formulation, 10 000 local ensembles were generated in a Monte-Carlo fashion and converted their elemental counts into the 15-feature vector required by the linear regressor. This procedure produced 2.81×10^6 local environments.

The predicted E_{ads}(CO) distribution of the equimolar AgAuCuPdPt HEA according to these Monte-Carlo generated adsorption site ensembles is shown in Fig. 4c with a closer look into the activity window -0.6 eV $< E_{ads}(CO) < -0.4$ eV. The E_{ads}(CO) follow the trend established by the DFT calculations Pt > Pd > Cu > Au > Ag (Fig. S6a). A noticeable shoulder on the stronger-binding side of each distribution (Fig. S6b) arises from the minority of CN = 6 corner sites in the icosahedral HEA nanoparticles. The results show that CN = 6 sites generally adsorb CO $\sim$ 0.20 eV more strongly than CN = 8 sites, underscoring how coordination plays a major role in binding. Notably, most configurations that satisfy -0.6 eV $< E_{ads}(CO) < -0.4$ eV are centered on Au atoms with CN = 8 or Ag atoms with CN = 6, whereas only a small subset of Cu-centered CN = 8 sites satisfy the E_{ads} range. Among the qualifying sites, Au (CN = 8) is the most abundant, hence we select these ensembles as the starting points for subsequent CO_2RR studies.

We then quantified, for each HEA composition, the fraction of Monte-Carlo site ensembles that satisfy the target range -0.6 eV $< E_{ads}(CO) < -0.4$ eV (Fig. S7 and S8). In the equimolar AgAuCuPdPt alloy only about 15% of the 10 000 sampled sites fall within this window (Fig. S7). That share rises as the Au or Ag content is increased with Au having the larger effect. Reducing the Pd and Pt fractions to 5 at% is even more beneficial: for $Ag_{30}Au_{30}Cu_{30}Pd_5Pt_5$ the proportion of "ideal" sites climbs to 24% (Fig. S8), and further Au enrichment pushes it higher still. Although simple, this Monte-Carlo workflow provides a rapid, quantitative glimpse of how bulk composition governs the distribution of E_{ads}(CO) and hence the density of catalytically relevant sites in HEA nanoparticles.

In summary, the Monte-Carlo screening highlights Au-centered facet sites (CN = 8) as the dominant contributors to the desired adsorption window -0.6 eV $< E_{ads}(CO) < -0.4$ eV. Ag corner sites (CN = 6) offer a secondary—though less abundant—contribution. Because these statistics reflect the coordination distribution of $\sim$1 nm (55-atom) icosahedra, they inherently capture nanoscale coordination effects. As particle size increases (fewer corners relative to facets), the prevalence of CN = 6 *vs.* CN = 8 sites and, therefore, the balance of "ideal" motifs will shift, so the composition trends reported here should be interpreted for the $\sim$1 nm regime. Guided by these distributions, we then selected representative local motifs especially with central Au(CN = 8), Ag(CN = 6) and Cu(CN = 8) atom that fall in the optimal window for explicit DFT exploration of *COOH and *CHO. We generated a dataset with 84 *COOH and 105 *CHO geometries to span the chemical diversity of the HEA surface.

3.3. CO_2 reduction on HEA nanoparticle sites

Building upon these CO adsorption insights, we next analyze the key steps in the CO_2-to-CH_4 mechanism, *i.e.*, the formation of *COOH and *CHO intermediates. On a Cu_{55} NP, for instance, the most energy-intensive steps are $CO_2 + [e^- + H^+] \rightarrow$ *COOH (ΔE_1) and *CO + $[e^- + H^+] \rightarrow$ *CHO (ΔE_3). A stronger binding of *COOH lowers ΔE_1 because CO_2, $[e^- + H^+]$, and the clean NP serve as fixed references. In contrast, ΔE_3 depends on the stability of both *CO and *CHO, meaning that stronger binding of *CHO combined with moderate binding of *CO can lead to a lower ΔE_3. Over metals such as Pt or Pd, strong *COOH binding can indeed reduce ΔE_1, but because *CO and *CHO are also bound strongly, this does not necessarily imply a low ΔE_3.

Given the importance of these steps in dictating the overall reaction kinetics, we evaluated *via* DFT the stability of 84 *COOH and 105 *CHO adsorption configurations on various adsorption sites of the eight HEA nanoparticles shown in Fig. 3. Each adsorbate was positioned so that its carbon atom sampled a range of binding sites on the HEA nanoparticles, exploring multiple initial geometries. Along with our previously collected *CO data, these results enable us to compute the formation energies of *COOH, *CO, *CHO (eqn (2)–(5) of the Methodology section). For completeness, we also evaluated the competing *CO $\rightarrow$ *COH route by optimizing bridge/hollow *COH configurations on several site instances of the same eight NPs across multiple motifs. The reaction energy of the *CO $\rightarrow$ *COH PCET step remained higher than *CO $\rightarrow$ *CHO, confirming the *CHO pathway as preferred (Fig. S9).

3.3.1. General trends on the stability of *COOH, *CO, and *CHO on HEA sites. We compiled box-plot statistics of the formation energies of *COOH, *CO, and *CHO, revealing broad energy distributions across different local environments and metals, Fig. S10. As expected, the formation energies generally follow Pt < Pd < Cu < Au < Ag, indicating that Pt and Pd bind these intermediates more strongly. Across all sites, the *COOH + $[e^- + H^+] \rightarrow$ *CO + H_2O step (ΔE_2) is exothermic, rendering it unlikely to be rate-limiting. By contrast, the *CO_2 + $[e^- + H^+] \rightarrow$ *COOH step (ΔE_1) is endothermic over Ag, Au, and Cu, approximately thermoneutral over Pd ($\Delta E_1 \approx 0$ eV), and exothermic over Pt ($\Delta E_1 < 0$ eV).

Comparatively, *CO + [e^- + H^+] → *CHO (ΔE_3) is more challenging for Pd and Pt. The box-plot statistics of Fig. S10 suggest that *CO_2 + [e^- + H^+] → *COOH may be potential-limiting over Ag and Au sites, while the *CO + [e^- + H^+] → *CHO step is potential-limiting on Cu, Pd, and Pt sites. Notably, ΔE_3 appears to reach its lowest average values over Au (Fig. S11), suggesting that both *COOH and *CHO can form with moderate reaction energies on Au-based sites, highlighting Au's potential for facilitating the conversion of CO_2 into *CHO.

Coupling these results with the ones presented in the previous sections, Au sites with high coordination (CN = 8) stand out as the most promising sites for the CO_2RR. In the following section, we demonstrate that Au (CN = 8)–Cu (CN = 6) pairs lower the reaction energies forming *COOH, ΔE_1, and *CHO, ΔE_3. Mechanistically, the Au center (CN = 8) binds the carbon atom with moderate strength, while a neighboring Cu corner (CN = 6) anchors the oxygen, enabling bidentate stabilization of *COOH and *CHO. Because the surrogate encodes only the identity of the binding atom and the composition of its first coordination shell, we used it to prioritize candidates, and other long-range effects were probed by DFT. Tier-1 highlighted Au-centered CN = 8 sites as the most frequent within the −0.6 to −0.4 eV window, and Tier-2 DFT investigated those ML-nominated sites for neighbor and coordination effects. In this two-step workflow, the Au(CN = 8)–Cu(CN = 6) motif emerged from targeted DFT rather than from any assumption hard-coded in the model.

3.3.2. Stability of *COOH and *CHO on Au–Cu sites. To demonstrate the exceptional ability of Au (CN = 8)–Cu (CN = 6) pairs to stabilize *COOH and *CHO, we selected multiple Au sites on the most stable nanoparticle (A, Fig. 3a) and tested various orientations of these adsorbates. Both *COOH and *CHO can bind in monodentate (carbon-only) or bidentate (carbon and oxygen) configurations, and we observed that bidentate adsorption generally provides stronger stabilization. Moreover, the identity and local environment of the metal binding the adsorbate's oxygen atom is critical to lower ΔE_1 and ΔE_3. Across the eight selected 55-atom icosahedral isomers we examined, this Au(CN = 8)–Cu(CN = 6) motif appears in 7 of 8 structures (including the global minimum; Table S2), indicating thermodynamic accessibility. Establishing its persistence under electrochemical bias and solvation will require future constant-potential/explicit-electrolyte studies.

As an example (Fig. S12), we examined *COOH and *CHO adsorbed on the same Au site in three ways: (1) monodentate binding, (2) bidentate with the oxygen atom bound to a neighboring Pt (CN = 6), and (3) bidentate with the oxygen atom bound to a neighboring Cu (CN = 6). In the *COOH case, bidentate adsorption with O–Cu (CN = 6) is most favorable, yielding ΔE_1 = 0.03 eV, compared to ΔE_1 = 0.31 eV for the O–Pt bidentate configuration and ΔE_1 = 0.45 eV for monodentate binding. A similar trend emerges for *CHO: the bidentate O–Cu configuration results in ΔE_3 = −0.06 eV, which is 0.28 eV and 0.27 eV more favorable than the bidentate O–Pt and monodentate cases, respectively. Most remarkably, this Au–Cu site renders both ΔE_1 and ΔE_3 to near zero, which would translate in practice to a required minimum applied potential. We note that as these elementary steps become near thermoneutral, other steps in the mechanism may become potential-limiting.

We further confirmed that both metal identity and local coordination influence stabilizing ability. In another test (Fig. S13), we placed *COOH and *CHO in bidentate modes on an Au (CN = 8) site neighbored by two Cu atoms, one with CN = 6 and another with CN = 8. Adsorption where the intermediate's oxygen binds to Cu (CN = 6) yields ΔE_1 = 0.16 eV and ΔE_3 = −0.10 eV, which are 0.36 eV and 0.35 eV more favorable, respectively, than binding to Cu (CN = 8). Hence, the synergy of Au (CN = 8)–Cu (CN = 6) arises from their complementary coordination environments as well as their distinct metal identities. Prior studies[6,7] have shown that a second catalytic center can disrupt the scaling relationships, presumably enhancing the efficiency of the catalyst.[10,11] We also tested other sites within the ideal E_{ads}(CO) window (−0.6 eV to −0.4 eV), Fig. S14; however, in the absence of a neighboring Cu (CN = 6) for bidentate stabilization, ΔE_1 and ΔE_3 remained above 0.2 eV.

We found that the Au(CN = 8)–Cu(CN = 6) pair breaks the conventional scaling relationship between *CO and *CHO energies and ΔE_3 can approach thermoneutrality or even become exothermic, Fig. 5. The contour lines in this figure indicate the values for ΔE_3 as a function of both the formation energy of *CO (E(*CO)) and *CHO (E(*CHO)). In most cases, the *CO + [e^- + H^+] → *CHO step, ΔE_3, is 0.3–0.9 eV endothermic in most cases, in agreement with the limit set by the CHO–CO scaling relation on pure metal as denoted by the green markers and corresponding green fitted line. Achieving $\Delta E_3 < 0$ eV at E_{ads}(CO) ∼ −0.5 eV would require *CHO formation energies lower than 0.2 eV, which is only possible at these special Au–Cu sites. As the datapoints representing specific Pt (dark blue) or Pd (light blue) sites illustrate, stabilizing *CHO intermediate is not enough to achieve a low ΔE_3. A balance between *CO and *CHO stabilization must be achieved.

We identified four configurations where $\Delta E_3 < 0$ eV, all corresponding to Au (CN = 8) sites adjacent to Cu (CN = 6). These sites also stabilize *COOH so that ΔE_1 remains below 0.2 eV (Fig. S15). Notably, the E_{ads}(CO) values on these datapoints are near the target activity window, indicating that while E_{ads}(CO) remains a useful descriptor for catalytic activity, it must be coupled with another parameter capturing the site's capacity to bind the oxygen atom of key intermediates like *COOH and *CHO. Carrying out the CO_2RR to methane over these special sites lowers the thermodynamic driving requirement: the limiting potential is −0.58 V for the Au(CN = 8)–Cu(CN = 6) site *versus* −0.90 V for Cu_{55} (Fig. S16). A reduction of −0.32 V in the bias needed to render all electrochemical steps thermoneutral or exergonic.

To further clarify Au's role and Au–Cu synergy, we replaced Au with Ag, Cu, or Pd at one of these special sites and recalculated *COOH, *CO, and *CHO adsorption energies (Fig. S17). The adsorption site has a neighboring Cu with CN = 6. Notably, linear scaling relationships re-emerge when Au is substituted and worse performance is obtained, *i.e.*, a

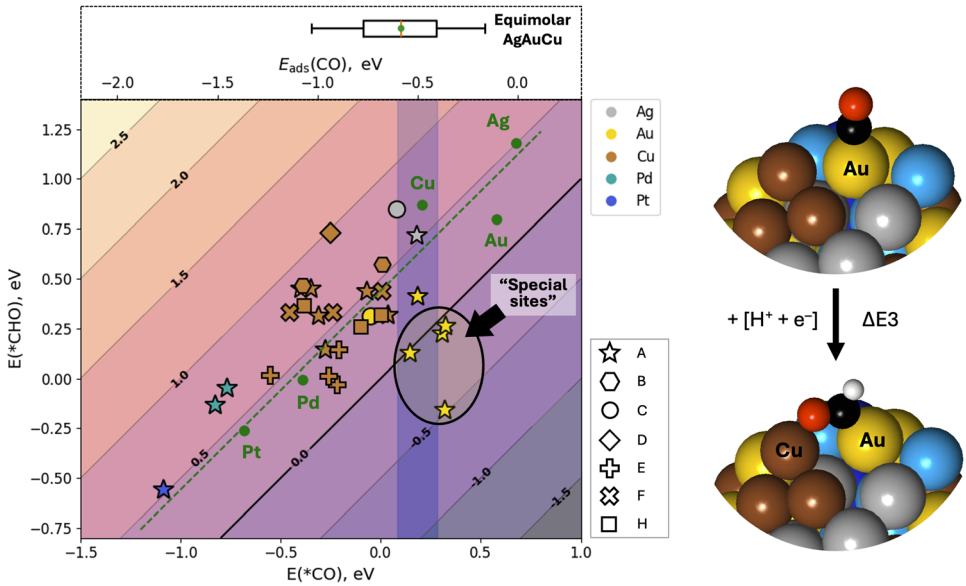

Fig. 5 Relationship between the formation energy of *CHO, E(*CHO) and the formation energy of *CO, E(*CO). The formation energies were calculated from the reference energies of gas-phase CO_2, H_2O, and H_2, and the energy of the corresponding NP following the computational hydrogen electrode scheme. Marker shape distinguishes the nanoparticle model, whereas marker color identifies the metal at the adsorption site center. The energy of reaction *CO + [H^+ + e^-] → *CHO is also given as the contour lines. The shaded region denotes the target E(*CO) which translates to E_{ads}(CO) between −0.6 eV and −0.4 eV. Above the secondary x-axis, a horizontal box plot summarizes the E_{ads}(CO) distribution for an equimolar 55-atom icosahedral Ag–Au–Cu nanoparticle (box = Q1–Q3; line = median; dot = mean; whiskers = 2.5th–97.5th percentiles). The DFT-calculated formation energies of *CHO and *CO on pure metal (111) surfaces are plotted as green markers, with their linear scaling relationship indicated by the green dashed line. For illustration, we also display the *CO and *CHO adsorption geometries on a representative "special site"—an Au atom with CN = 8 adjacent to a Cu atom with CN = 6.

higher ΔE_1 and ΔE_3. However, when Au is present, the data points lie well below the trendlines, confirming that specific Au–Cu pairs uniquely enable the breaking of standard scaling relationships and thus facilitates more efficient CO_2-to-CH_4 conversion.

Using the insights from the detailed DFT calculations together with the surrogate E_{ads}(CO) model, we re-examined the Monte-Carlo-generated site-ensemble grids described in the previous section that satisfy both of the following conditions: (i) -0.6 eV $< E_{ads}$(CO) < -0.4 eV, and (ii) an Au-centered surface atom (CN = 8) adjacent to at least one under-coordinated Cu corner atom (CN = 6). The resulting composition maps (Fig. S18 and S19) show that the equimolar $Ag_{20}Au_{20}Cu_{20}Pd_{20}Pt_{20}$ alloy contains only about 3% of such "Au(CN = 8)–Cu(CN = 6)" sites. Lowering Pd and Pt to 5 at% each and redistributing the excess equally between Ag, Au, and Cu ($Ag_{30}Au_{30}Cu_{30}Pd_5Pt_5$) increases this fraction to 8%. An apparent upper limit for sites satisfying the two conditions of about 20% resides near $Au_{55}Cu_{35}Pd_5Pt_5$, but whether such a composition remains single-phase will depend on entropic constraints. Beyond simply enriching Au and Cu, employing an HEA matrix offers practical advantages over conventional binary Au–Cu catalysts. Long-term stability for catalysis application is a challenge for Au–Cu binary nanoparticles and often additional technologies are required to maintain stability.[40] Dealloying[41] and oxidation of Cu[42] are part of the challenges. In contrast, embedding Au and Cu within a multielement HEA suppresses segregation and protects Cu from oxidation, while still delivering the Au(CN = 8)–Cu(CN = 6) motifs identified as catalytically active in this study.

Direct, coordination-resolved observation of the specific Au(CN = 8)–Cu(CN = 6) motif has not yet been reported, but multiple Au–Cu nanoparticle studies show behavior consistent with our picture (lower CO onset at smaller size, high CO selectivity in Au-enriched shells, and Au-modified Cu favoring *CO hydrogenation),[43–47] suggesting that adjacent Au/Cu ensembles are synthetically accessible and catalytically relevant. Because CN = 8 facet centers and CN = 6 corners co-occur on small icosahedra, decreasing particle size increases the statistical likelihood of forming Au(CN = 8)–Cu(CN = 6) pairs, in line with our Monte-Carlo trends. We also find this motif present in 7 out 8 icosahedral nanoparticles used in this study (Table S2), supporting its thermodynamic plausibility on nanoparticles. We therefore present such site motifs as an experimental target for synthesis and operando verification, rather than as evidence that it already delivers low-voltage CH_4 under device conditions.

3.4. Insight to the hydrogen evolution reaction (HER)

The HER competes with CO_2RR, potentially diverting current toward H_2 formation and reducing proton availability for carbon-based products. We assessed E_{ads}(H) as a HER activity descriptor, as previous volcano plot analysis suggests an ideal E_{ads}(H) near 0 eV to favor carbon-species reduction over HER.[48] Various 2-fold and 3-fold H adsorption configurations were

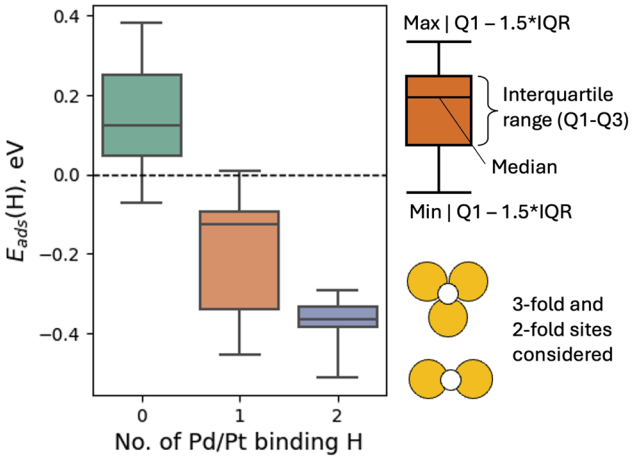

Fig. 6 Adsorption energy of H (E_{ads}(H)) over HEA nanoparticle A, and its dependence with the number of Pd or Pt involved in the binding of H. Only 2-fold (bridge) and 3-fold hollow sites considered.

examined at the most stable HEA NP (A) at multiple binding sites.

As shown in Fig. 6, E_{ads}(H) spans about 1 eV depending on the site and configuration. When Pd or Pt are present in the adsorption site, E_{ads}(H) falls below 0 eV, indicating strong H binding that promotes HER. Thus, even minor Pd or Pt content can create favorable HER sites, diminishing CO_2RR activity.

It is also possible that the subsurface Pd or Pt may migrate to the surface under CO/H conditions due to their stronger Pd/Pt–H/CO bonding compared to Au, Ag, Cu. Thus, replacing Pd or Pt with metals that bind H and CO less strongly could yield a more selective catalyst.

3.5. Limitations and outlook

As proposed in this work, HEAs have potential to deliver encouraging activity for a variety of applications. They have been explored for water splitting,[17] methanol oxidation,[49,50] oxygen reduction,[16] hydrogen evolution[19,50] and CO_2/CO reduction.[14,51] However, their long-term stability remains far less explored than their activity. The AgAuCuPdPt system examined in this work has been experimentally synthesized and tested for hydrogen sensing,[52] electro-oxidation of formic acid and methanol,[49] and CO_2 electroreduction to hydrocarbons.[14] In the latter study, ~16 nm HEA nanoparticles sustained steady-state CO_2RR activity during a 5 h chronoamperometry test in 0.5 M K_2SO_4. Promising, but still short of the durability benchmarks required for practical devices.

Priamushko *et al.* have emphasized that improved stability is often assumed for HEAs but not rigorously proven.[53] Real electrolyzers operate under high current densities, variable pH, and complex electrolytes; kinetic processes such as dissolution and surface reconstruction can override the thermodynamic benefits of high configurational entropy. *In situ* characterization through a scanning flow cell coupled to an inductively coupled plasma mass spectrometer (SFC/ICP-MS), recently showed lower metal dissolution for multimetal systems, but largely attributable to simple dilution rather than intrinsic "entropy stabilization", challenging any purely thermodynamic standpoint.[54] Conversely, Au enrichment has been reported to enhance durability in both single-metal[55] and multimetal electrocatalysts.[56,57] These mixed findings underscore the need for systematic, long-duration tests at industrial current densities, complemented by operando and post-mortem compositional analyses.

Our modelling delivers atom-level insight into activity trends, yet several limitations must be acknowledged. First, the DFT calculations were performed in vacuum, so effects such as explicit solvent, specific ion adsorption and double-layer fields were not considered. These factors could potentially influence adsorption geometries and surface dipoles. The fixed charge approach was used in this work; thus, the applied bias was introduced through the computational hydrogen-electrode formalism. Consequently, field-induced reconstructions that may occur at large potentials are not captured in this approach, and thus, remain beyond the scope of our current study. In addition, we confined the structural space to 55-atom icosahedral nanoparticles: larger particles or alternative shapes will alter the fraction of corner (CN = 6) and edge (CN = 8) sites and could therefore shift the population of the Au(CN = 8)–Cu(CN = 6) motif. Finally, possible metal dissolution or redeposition under operating conditions was not modelled, so kinetic corrosion effects are absent. Addressing these points requires a multiscale strategy such as constant-potential *ab initio* molecular dynamics (AIMD)[58,59] or grand-canonical DFT to include electrolyte,[60] kinetic Monte-Carlo to follow segregation and leaching,[61,62] and operando X-ray absorption spectroscopy[19] or liquid-phase transmission electron microscopy[63] to verify whether the predicted motifs persist, evolve, or self-heal in real CO_2-electrolysis environments.

4. Conclusions

We conducted a combined ML model and DFT calculations to investigate AgAuCuPdPt HEA nanoparticles for CO_2-to-CH_4 conversion. By training a linear model on DFT-calculated CO adsorption configurations on the HEA's nanoparticles, we achieved state-of-the-art predictive accuracy, allowing us to screen millions of Monte-Carlo-generated local atomic environments distributed over 281 HEA formulations. Based on the well-established E_{ads}(CO) descriptor, this high-throughput scan showed that increasing the Au fraction, specially of edge sites with CN = 8, is the most effective way to raise the population of "ideal" sites (-0.6 eV $< E_{ads}(CO) < -0.4$ eV), with Ag (CN = 6) contributing to a smaller scale. A composition such as $Ag_{30}Au_{30}Cu_{30}Pd_5Pt_5$ doubles the fraction of ideal sites relative to the equimolar alloy.

Targeted DFT calculations then revealed that Au (CN = 8) sites adjacent to Cu (CN = 6) sites break conventional scaling relationships. These uniquely structured Au–Cu environments can lower reaction barriers and surpass the limitations predicted by volcano-plot analyses, indicating tailored local atomic arrangements can surpass conventional catalytic limitations. Re-examining the Monte-Carlo-generated local environments

and filtering for both optimal E_{ads}(CO) and the Au–Cu motif showed that their abundance rises from ~3% in the equimolar alloy to ~8% when Pd and Pt are reduced to 5% each and could reach a theoretical maximum (~20%) near $Au_{55}Cu_{35}Pd_5Pt_5$. Because Pd and Pt also create strong H-binding sites that favor HER, omitting or minimizing these elements not only boosts the count of Au–Cu active motifs but also improves selectivity.

Overall, our results suggest that high-entropy alloys can be tuned in both composition and local coordination, potentially breaking linear scaling constraints and balancing key intermediate adsorption. These findings underscore the promise of HEAs for electrocatalytic CO_2RR and provide a practical framework—combining ML-based screening with targeted DFT simulations—for discovering next-generation catalysts that deliver high activity and selectivity. Thus the present study should be viewed as a predictive, kinetics-oriented roadmap that identifies promising compositions and motifs for forthcoming experimental studies.

Conflicts of interest

There are no conflicts to declare.

Data availability

Additional figures and tables supporting this article are included as part of the supplementary information (SI). The SI also includes an analysis of the structural and energetic stability of all 120 55-atom icosahedral HEA nanoparticles, the filtering procedure applied to the CO adsorption dataset for surrogate model training, and the generation of 10 000 adsorption-site ensembles used to derive composition-weighted Monte-Carlo statistics of CO adsorption energies. See DOI: **https://doi.org/10.1039/d5mh01064k**

The datasets (including atomic structures) and the code used for analysis is available on GitHub at **https://github.com/compcatalgroupIHPC/hea-co2rr-breaking-scaling.git**.

Acknowledgements

This work is supported by the Agency for Science, Technology and Research (A*STAR) under the RIE 2025 MTC programmatic fund (grant no. M24N4b0034), the Singapore National Research Foundation's Competitive Research Program funding (NRF-CRP23-2019-0001), and RIE2025 USS LCER Phase 2 Programme HETFI Directed Hydrogen Programme (Grant No. U2305D4001). Q. T. T. would like to acknowledge the financial support by the project under the Australian Research Council (FL230100023). The authors acknowledge the National Supercomputing Centre (NSCC) Singapore and A*STAR Computational Resource Centre (A*CRC) for the use of its high-performance computing facilities.

References

1 Y. Hori, K. Kikuchi and S. Suzuki, *Chem. Lett.*, 1985, 1695–1698.
2 Y. Hori, A. Murata and R. Takahashi, *J. Chem. Soc., Faraday Trans. 1*, 1989, **85**, 2309.
3 K. P. Kuhl, E. R. Cave, D. N. Abram and T. F. Jaramillo, *Energy Environ. Sci.*, 2012, **5**, 7050.
4 Z. Zhang, E. W. Lees, S. Ren, B. A. W. Mowbray, A. Huang and C. P. Berlinguette, *ACS Cent. Sci.*, 2022, **8**, 749–755.
5 M. Dorn, F. Frantzen, S. Kareth, E. Weidner and M. Petermann, *Ind. Eng. Chem. Res.*, 2025, **64**, 10056–10069.
6 M. Jouny, W. Luc and F. Jiao, *Ind. Eng. Chem. Res.*, 2018, **57**, 2165–2177.
7 J. K. Nørskov, T. Bligaard, J. Rossmeisl and C. H. Christensen, *Nat. Chem.*, 2009, **1**, 37–46.
8 F. Abild-Pedersen, J. Greeley, F. Studt, J. Rossmeisl, T. R. Munter, P. G. Moses, E. Skúlason, T. Bligaard and J. K. Nørskov, *Phys. Rev. Lett.*, 2007, **99**, 016105.
9 R. Michalsky, Y. J. Zhang, A. J. Medford and A. A. Peterson, *J. Phys. Chem. C*, 2014, **118**, 13026–13034.
10 P. Wang, F. Chang, W. Gao, J. Guo, G. Wu, T. He and P. Chen, *Nat. Chem.*, 2017, **9**, 64–70.
11 Z. W. Chen, Z. Gariepy, L. Chen, X. Yao, A. Anand, S.-J. Liu, C. G. Tetsassi Feugmo, I. Tamblyn and C. V. Singh, *ACS Catal.*, 2022, **12**, 14864–14871.
12 A.-I. Hutu, E. Pervolarakis, I. N. Remediakis, H. H. Kristoffersen and J. Rossmeisl, *J. Phys. Chem. C*, 2024, **128**, 10251–10258.
13 J. Chen and Y. Ji, *Chin. J. Catal.*, 2022, **43**, 2889–2897.
14 S. Nellaiappan, N. K. Katiyar, R. Kumar, A. Parui, K. D. Malviya, K. G. Pradeep, A. K. Singh, S. Sharma, C. S. Tiwary and K. Biswas, *ACS Catal.*, 2020, **10**, 3658–3663.
15 P. Xie, Y. Yao, Z. Huang, Z. Liu, J. Zhang, T. Li, G. Wang, R. Shahbazian-Yassar, L. Hu and C. Wang, *Nat. Commun.*, 2019, **10**, 4011.
16 K. Wang, R. Chen, H. Yang, Y. Chen, H. Jia, Y. He, S. Song and Y. Wang, *Adv. Funct. Mater.*, 2024, **34**, 1–9.
17 J. Kwon, S. Sun, S. Choi, K. Lee, S. Jo, K. Park, Y. K. Kim, H. B. Park, H. Y. Park, J. H. Jang, H. Han, U. Paik and T. Song, *Adv. Mater.*, 2023, **35**, 1–11.
18 R. Reske, H. Mistry, F. Behafarid, B. Roldan Cuenya and P. Strasser, *J. Am. Chem. Soc.*, 2014, **136**, 6978–6986.
19 H. Cai, H. Yang, S. He, D. Wan, Y. Kong, D. Li, X. Jiang, X. Zhang, Q. Hu and C. He, *Angew. Chem., Int. Ed.*, 2025, **64**, e202423765.
20 Y. Li, Z. Yao, W. Gao, W. Shang, T. Deng and J. Wu, *Small*, 2024, **20**, 1–19.
21 P. E. Blöchl, *Phys. Rev. B: Condens. Matter Mater. Phys.*, 1994, **50**, 17953–17979.
22 B. Hammer, L. B. Hansen and J. K. Nørskov, *Phys. Rev. B: Condens. Matter Mater. Phys.*, 1999, **59**, 7413–7421.
23 J. K. Nørskov, J. Rossmeisl, A. Logadottir, J. R. Kitchin, T. Bligaard and H. Jónsson, *J. Phys. Chem. B*, 2024, **108**, 17886–17892.
24 T. L. Tan, L.-L. Wang, D. D. Johnson and K. Bai, *Nano Lett.*, 2012, **12**, 4875–4880.
25 T. L. Tan, L.-L. Wang, J. Zhang, D. D. Johnson and K. Bai, *ACS Catal.*, 2015, **5**, 2376–2383.
26 N. A. Zarkevich, T. L. Tan and D. D. Johnson, *Phys. Rev. B: Condens. Matter Mater. Phys.*, 2007, **75**, 104203.

27 A. Zunger, S.-H. Wei, L. G. Ferreira and J. E. Bernard, *Phys. Rev. Lett.*, 1990, **65**, 353–356.
28 Z. Leong, U. Ramamurty and T. L. Tan, *Acta Mater.*, 2021, **213**, 116958.
29 Z. Leong, H. Jin, Z. M. Wong, K. Nemani, B. Anasori and T. L. Tan, *Chem. Mater.*, 2022, **34**, 9062–9071.
30 Z. Leong and T. L. Tan, *Phys. Rev. B*, 2019, **100**, 134108.
31 N. A. Zarkevich and D. D. Johnson, *Phys. Rev. Lett.*, 2004, **92**, 255702.
32 Z. M. Wong, T. L. Tan, S.-W. Yang and G. Q. Xu, *J. Phys.: Condens. Matter*, 2018, **30**, 485402.
33 J. P. K. Doye and D. J. Wales, *New J. Chem.*, 1998, **22**, 733–744.
34 F. Baletto and R. Ferrando, *Rev. Mod. Phys.*, 2005, **77**, 371–423.
35 A. A. Peterson and J. K. Nørskov, *J. Phys. Chem. Lett.*, 2012, **3**, 251–258.
36 A. Patra, H. Peng, J. Sun and J. P. Perdew, *Phys. Rev. B*, 2019, **100**, 035442.
37 K. P. Kuhl, T. Hatsukade, E. R. Cave, D. N. Abram, J. Kibsgaard and T. F. Jaramillo, *J. Am. Chem. Soc.*, 2014, **136**, 14107–14113.
38 M. Rittiruam, P. Khamloet, A. Ektarawong, C. Atthapak, T. Saelee, P. Khajondetchairit, B. Alling, S. Praserthdam and P. Praserthdam, *Appl. Surf. Sci.*, 2024, **652**, 159297.
39 B. M. Wood, M. Dzamba, X. Fu, M. Gao, M. Shuaibi, L. Barroso-Luque, K. Abdelmaqsoud, V. Gharakhanyan, J. R. Kitchin, D. S. Levine, K. Michel, A. Sriram, T. Cohen, A. Das, A. Rizvi, S. J. Sahoo, Z. W. Ulissi and C. L. Zitnick, *arXiv*, 2025, preprint, arXiv:2506.23971, DOI: 10.48550/arXiv.2506.23971.
40 X. Mi, H. Chen, J. Li and H. Qiao, *Front. Chem.*, 2023, **11**, 1–11.
41 T. P. Moffat, F. F. Fan and A. J. Bard, *J. Electrochem. Soc.*, 1991, **138**, 3224–3235.
42 Y. Guan, Y. Liu, Q. Ren, Z. Dong and L. Luo, *Nano Res.*, 2023, **16**, 2119–2125.
43 X. Wang, P. Ou, J. Wicks, Y. Xie, Y. Wang, J. Li, J. Tam, D. Ren, J. Y. Howe, Z. Wang, A. Ozden, Y. Z. Finfrock, Y. Xu, Y. Li, A. S. Rasouli, K. Bertens, A. H. Ip, M. Graetzel, D. Sinton and E. H. Sargent, *Nat. Commun.*, 2021, **12**, 3387.
44 J. Huang, J. Dai, J. Zhu, R. Chen, X. Fu, H. Liu and G. Li, *J. Catal.*, 2022, **415**, 134–141.
45 S. Dai, T.-H. Huang, W.-I. Liu, C.-W. Hsu, S.-W. Lee, T.-Y. Chen, Y.-C. Wang, J.-H. Wang and K.-W. Wang, *Nano Lett.*, 2021, **21**, 9293–9300.
46 E. Andrews, Y. Fang and J. Flake, *J. Appl. Electrochem.*, 2018, **48**, 435–441.
47 D. Kim, C. Xie, N. Becknell, Y. Yu, M. Karamad, K. Chan, E. J. Crumlin, J. K. Nørskov and P. Yang, *J. Am. Chem. Soc.*, 2017, **139**, 8329–8336.
48 A. Bagger, W. Ju, A. S. Varela, P. Strasser and J. Rossmeisl, *Chem. Phys. Chem.*, 2017, **18**, 3266–3273.
49 N. K. Katiyar, S. Nellaiappan, R. Kumar, K. D. Malviya, K. G. Pradeep, A. K. Singh, S. Sharma, C. S. Tiwary and K. Biswas, *Mater. Today Energy*, 2020, **16**, 100393.
50 H. Li, Y. Han, H. Zhao, W. Qi, D. Zhang, Y. Yu, W. Cai, S. Li, J. Lai, B. Huang and L. Wang, *Nat. Commun.*, 2020, **11**, 1–9.
51 J. K. Pedersen, T. A. A. Batchelor, A. Bagger and J. Rossmeisl, *ACS Catal.*, 2020, **10**, 2169–2176.
52 K. M. B. Urs, N. K. Katiyar, R. Kumar, K. Biswas, A. K. Singh, C. S. Tiwary and V. Kamble, *Nanoscale*, 2020, **12**, 11830–11841.
53 T. Priamushko, A. Kormányos and S. Cherevko, *Curr. Opin. Chem. Eng.*, 2024, **44**, 101020.
54 A. Kormányos, Q. Dong, B. Xiao, T. Li, A. Savan, K. Jenewein, T. Priamushko, A. Körner, T. Böhm, A. Hutzler, L. Hu, A. Ludwig and S. Cherevko, *iScience*, 2023, **26**, 107775.
55 J. Zhang, K. Sasaki, E. Sutter and R. R. Adzic, *Science*, 2007, **315**, 220–222.
56 L. Guo, D. Zhang and L. Guo, *Adv. Funct. Mater.*, 2020, **30**, 1–8.
57 K. Sasaki, H. Naohara, Y. Choi, Y. Cai, W.-F. Chen, P. Liu and R. R. Adzic, *Nat. Commun.*, 2012, **3**, 1115.
58 H. D. Jung, G. Yu, H. J. Kim and S. Back, *ChemRxiv*, 2025, preprint, DOI: 10.26434/chemrxiv-2025-mdblc.
59 H. Cao, X. Lv, S. Qian, J. Li and Y.-G. Wang, *J. Phys. Chem. Lett.*, 2024, **15**, 1314–1320.
60 M. M. Melander, M. J. Kuisma, T. E. K. Christensen and K. Honkala, *J. Chem. Phys.*, 2019, **150**, 041706.
61 F. Calvo, *Faraday Discuss.*, 2025, DOI: 10.1039/D5FD00077G.
62 Q. Ye, B. Yang, G. Yang, J. Zhao and Z. Gong, *Mater. Lett.*, 2022, **306**, 130907.
63 J. Sun, A. Leff, Y. Li and T. J. Woehl, *Nanoscale*, 2023, **15**, 10447–10457.